



Effect of graphene dispersion on the equilibrium structure and deformation of graphene/eicosane composites as surrogates for graphene/polyethylene composites: a molecular dynamics simulation

Shenghui Chen¹, Qiang Lv¹, Zhikun Wang¹, Chunling Li¹, Charles U. Pittman Jr.², Steven R. Gwaltney², Shuangqing Sun^{1,*}, and Songqing Hu^{1,3,*}

¹ College of Science, China University of Petroleum (East China), Qingdao 266580, People's Republic of China

² Department of Chemistry, Mississippi State University, Mississippi State, MS 39762, USA

³ Key Laboratory of New Energy Physics and Materials Science in Universities of Shandong, China University of Petroleum (East China), Qingdao 266580, China

Received: 22 November 2016

Accepted: 13 January 2017

Published online:
23 January 2017

© Springer Science+Business
Media New York 2017

ABSTRACT

Molecular dynamics simulations are used to investigate the effect of graphene dispersion on the equilibrium structure and deformation of graphene/eicosane composites. Two graphene sheets with four different interlayer distances are incorporated, respectively, into a eicosane matrix to form graphene/eicosane composites representing different graphene dispersions. With greater graphene dispersion, the “adsorption solidification” of the eicosane increases, where eicosane molecular lamination, orientation, and extension become more uniform and stronger. In addition, eicosane molecular motion is inhibited more in the direction perpendicular to graphene surfaces. When these graphene/eicosane composites are deformed, the free volume initially increases slowly due to small, scattered voids. After reaching the yield strains, the free volume rises sharply as the structures of composites are damaged, and small voids merge into large voids. The damage always occurs in the region of the composite with the weakest “adsorption solidification.” Since this effect is stronger when the graphene sheets are more dispersed, more complete dispersion results in higher composite yield stresses. Lessons from these simulations may provide some insights into graphene/polyethylene composites, where suitable models would require very long equilibration times.

Address correspondence to E-mail: sunshuangqing@upc.edu.cn; songqinghu@upc.edu.cn

Introduction

Since graphene was discovered using the simple Scotch tape method [1], it has attracted significant attention based on its superior properties [2–4]. Composites filled with graphene have been widely investigated to enhance mechanical, electrical, and thermal properties [5–8]. In the past few years, graphene sheets have been incorporated into a wide range of polymer matrices [9–13]. Graphene fillers can improve the fracture and fatigue resistance of epoxy polymers to the same degree as carbon nanotube (CNT), but the weight fraction of graphene needed was one to two orders of magnitude lower compared with CNTs [14, 15]. These unusual mechanical properties make graphene-based composites attractive for a wide range of potential applications.

Obtaining a uniform and homogeneous graphene dispersion in the matrix is a key issue to achieve optimal properties of graphene-based composites. Graphene sheets usually aggregate and stack within the host matrix under the influence of van der Waals forces and strong π - π interactions [16, 17]. The reported cleavage energy of graphite was about 61 meV/atom [18]. The poor graphene dispersion in a matrix strongly limits the performance and the application of graphene-based composites. Tang et al. [19] investigated graphene/epoxy composites prepared with different dispersions of graphene sheets. Composite samples with highly dispersed reduced graphene oxide (RGO) showed higher strengths and higher glass transition temperatures than the composites with poorly dispersed RGO. Kim et al. [20] compared three different dispersion methods: solvent blending, in situ polymerization, and melt compounding for fabricating thermoplastic polyurethane (TPU) reinforced with exfoliated graphite. The TPU offered the best conductivity, Young's modulus, and N_2 permeability after solvent blending, which was the method that resulted in the highest dispersion. Yang et al. [21] investigated the synergetic effects between multi-sheet graphitic platelets and multi-walled carbon nanotubes. Multi-walled carbon nanotubes inhibited the aggregation of multi-sheet graphitic platelets. Therefore, the epoxy composites with both carbon nanotubes and graphitic plates exhibited better mechanical properties and thermal conductivity.

Although many experimental studies have been conducted in this field, experimental studies of the

graphene dispersion effects within composites at the atomic/molecular level and of the mechanistic effects are very difficult. In the past few years, computational simulations have been applied in the graphene-based composites as a useful tool to study the behavior of materials at the atomic/molecular level [22–28]. To date, most of these graphene composite computational simulations focused on composite properties and the interactions between graphene and host molecules [22–24]. Conversely, the simulations of the effects of graphene dispersion are scarce and simple. Shiu et al. [25] investigated the mechanical and thermal properties of graphene/epoxy nanocomposites using either graphene flakes or intercalated graphene. Nanocomposites with intercalated graphene exhibited higher Young's moduli, higher glass transition temperatures, and lower thermal expansion coefficients than those with graphene flakes. The intercalated graphene led to a higher amount of high-density polymer within the nanocomposites. However, the models in their work were simple, and the analysis of the dispersion effects was not adequate. Also, the model sizes used for the dispersed and the aggregated graphene sheets were too different to reasonably compare in their work. Rahman et al. [26] investigated the mechanical properties of composites with different graphene dispersions and spatial arrangements [27]. Mechanical deformation was performed to analyze the mechanical properties and the failure mechanism of these composites. The dispersed graphene enhanced the in-plane elastic modulus more than agglomerated graphene. However, the effect of graphene dispersion on failure mechanism was not deeply analyzed.

Hadden et al. [28] studied the mechanical performance of graphene nanoplatelets/carbon fiber/epoxy hybrid composites using a multiscale modeling approach, including molecular dynamics simulations and micromechanical modeling. The experimental testing results proved that this multiscale modeling approach was accurate. Several models with different graphene nanoplatelet dispersions were simulated. The results showed that graphene nanoplatelet dispersion had a strong effect on the transverse tensile properties of the composite. Their work focused on developing the multiscale modeling approach and predicting the properties of composite. However, the micro-behavior of the host molecules during the deformation and the impact mechanism of graphene dispersion were not deeply

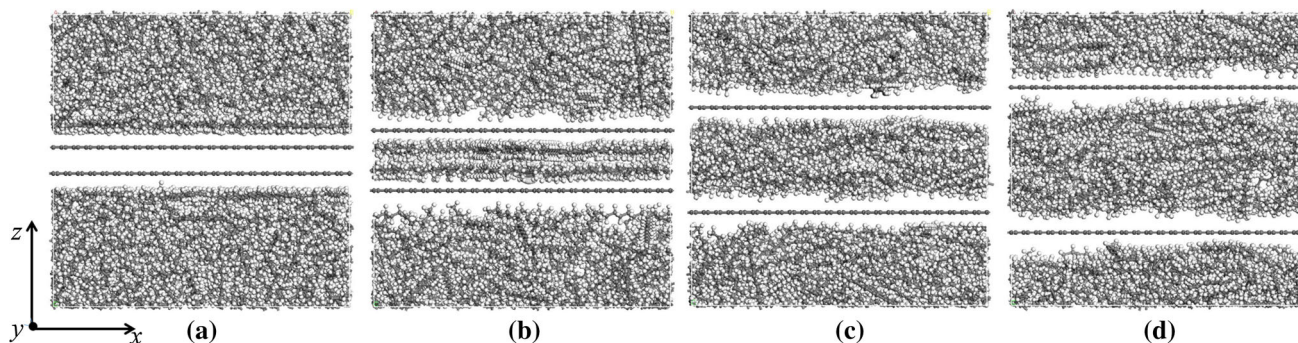


Figure 1 View of the initial models with different graphene dispersions in eicosane. The distance between the graphene sheets are 3.4 Å for model A (a), 10.2 Å for model B (b), 18.0 Å for model C (c), and 25.0 Å for model D (d), respectively.

discussed. On the whole, the effect of graphene dispersion is relatively unexplored, and dispersion influences on the mechanism of failure remain an important open question.

In the present work, molecular dynamics (MD) simulations were used to study the effect of graphene dispersion on a graphene/eicosane matrix composite's equilibrium structure and how this structure changes during deformation. We built graphene/eicosane composites with four different graphene dispersions. The structural properties, the movements of the eicosane molecules, and the stress–strain behavior of the graphene/eicosane matrix composites during a uniaxial tensile process were analyzed and compared between these dispersions.

Calculation models and methods

Simulation models

In this work, the C-20 hydrocarbon eicosane ($\text{CH}_3-(\text{CH}_2)_{18}-\text{CH}_3$) and parallel graphene sheets were built as a modes of graphene/polyethylene composites (Fig. 1). Eicosane is serving as a surrogate for polyethylene to simplify simulations and to avoid excessive factors. Eicosane or another short linear aliphatic hydrocarbon chain has often been used in simulation models of polyethylene-based composites [29–34] when the effect of host molecule's length was not the focus and had little effect on the simulation results. Periodic boundary conditions were applied in the x , y , and z directions. The simulation cell size was $51.7 \text{ \AA} \times 51.1 \text{ \AA} \times 50.0 \text{ \AA}$. In the initial models, the density of the host matrix was set at 0.9 g cm^{-3} . The total numbers of atoms in all four models are 15,346, 15,780, 15,718, and 15,780 atoms, respectively. All the

initial structures were built using the Materials Studio software package.¹

Different graphene dispersions were simulated using two graphene sheets with different interlayer distances. The two graphene sheets with a 3.4 Å intersheet distance (model A) simulated the complete aggregation of graphene, since the two sheets were stacked together with no eicosane molecules between them. Then, the two graphene sheets were dispersed by increasing the interlayer distance to 10.2 Å in model B, 18.0 Å in model C and 25.0 Å in model D. Since the model size in the z -direction (perpendicular to the graphene surface) was 50.0 Å and the model was periodic, the 25.0 Å separation distance was the largest possible separation between two sheets in our model. Thus, model D was considered to be the structure with complete dispersion.

Dynamics simulations

All the molecular dynamics simulations in this work were carried out using LAMMPS (Large Scale Atomic/Molecular Massively Parallel Simulator) [35]. The polymer consistent force field (PCFF) [36] was applied. It has been previously validated for simulating mechanical properties [37, 38, 41]. The simulation timestep was 1 fs. A cutoff distance of 12.5 Å was used for all the simulations.

To obtain the equilibrium structures of graphene/eicosane composites, a series of dynamics simulations were performed. First, an NVT (constant volume, temperature, and number of particles) ensemble was used with a temperature of 300 K for 1 ns using the Nose–Hoover thermostat. The purpose of this

¹ Accelrys, Inc. <http://accelrys.com/products/materials-studio/> (date accessed: January 12, 2011).

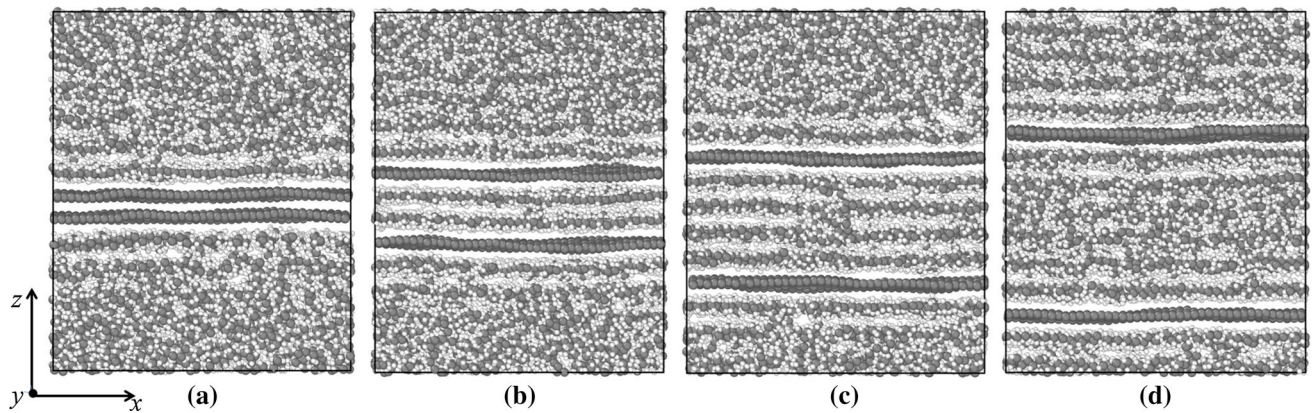


Figure 2 Equilibrium structures of models A (a), B (b), C (c), and D (d).

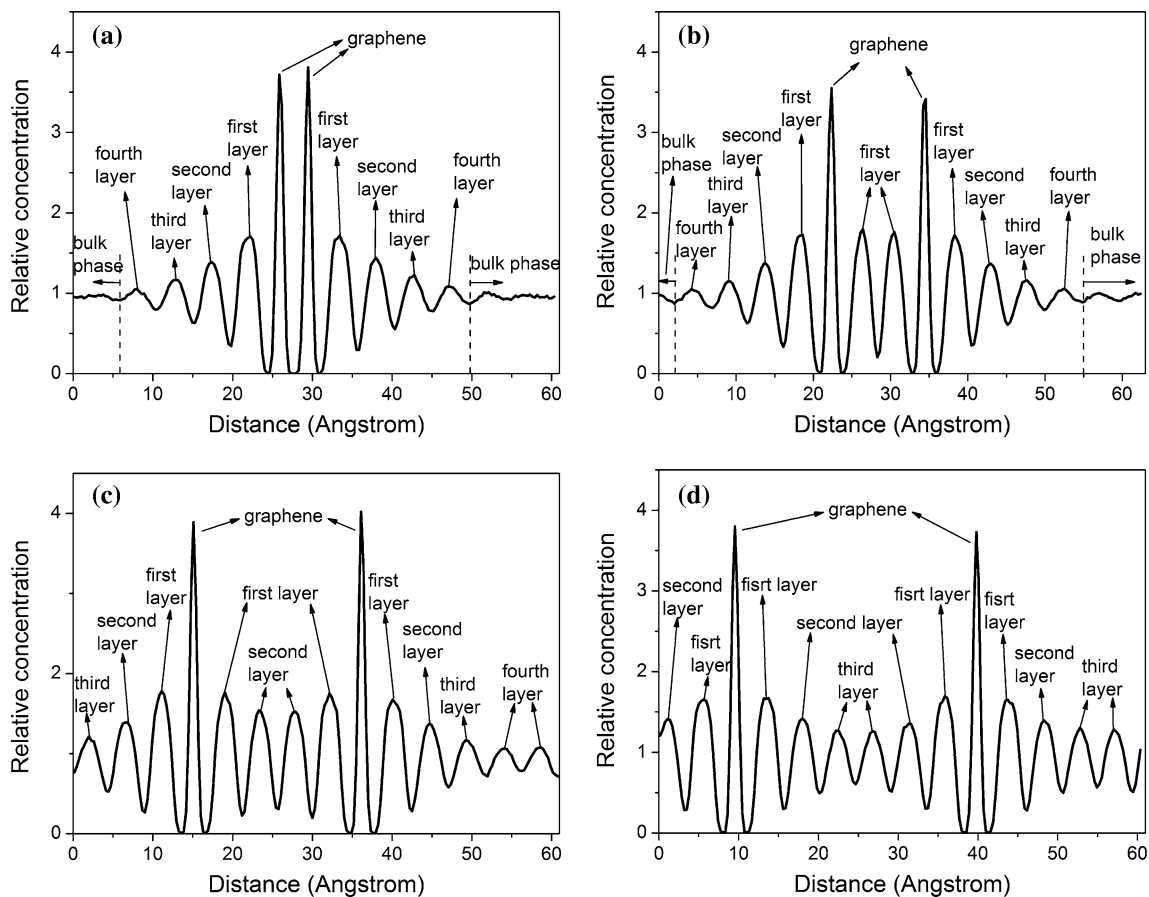


Figure 3 Relative concentration of the equilibrium structures for models A (a), B (b), C (c) and D (d).

simulation was to make the temperature stable at near room temperature. Second, an MD simulation was carried out for 3 ns within the NPT (constant pressure, temperature, and number of particles) ensemble with a pressure of 1 atm and temperature

of 300 K, using the Nose–Hoover barostat and thermostat. Third, another MD simulation with a NVT ensemble was run for 3 ns to ensure the structure’s equilibration. All the equilibrium structure analyses were obtained from the last 1 ns of the last NVT MD

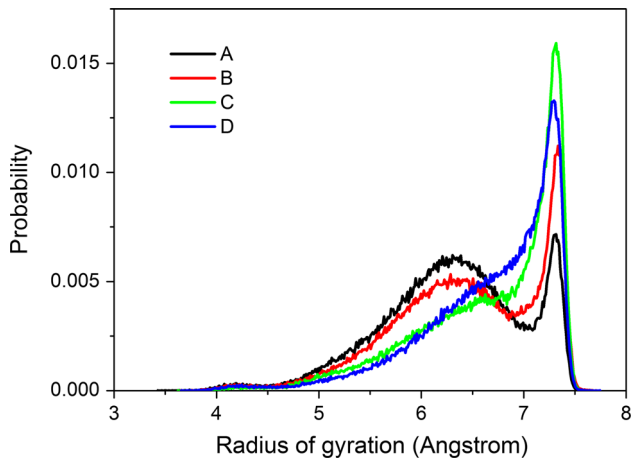


Figure 4 Distribution of radius of gyration for eicosane in four models.

simulations. The same procedure was used for all the four models.

Once the equilibration simulations were completed, the four models were subjected to uniaxial tensile simulations. The tensile process was carried out via non-equilibrium MD simulations. The models were deformed at a constant strain of $5 \times 10^8 \text{ s}^{-1}$ along the direction perpendicular to the graphene sheet surfaces (the z -direction) while maintaining atmospheric pressure in the other two transverse directions using Nose–Hoover barostat. This mixed-boundary conditions method was similar to the $\text{NTL}_x\text{S}_{yy}\text{S}_{zz}$ ensemble method proposed by Yang et al. [39]. The temperature used during the deformation process was also 300 K. The stress–strain curves for the four models fluctuated greatly because of the excessive thermal noise during the straining simulation at 300 K. Hossain et al. [40] investigated the temperature effect on the deformation of polyethylene. Their results also showed that the thermal noise was much larger when the temperature was higher. In order to avoid the thermal noise, Jiang et al. [41] reduced the temperature to 0.01 K in a similar deformation simulation of composites. However, the temperature of 0.01 K was too low to simulate a real deformation, since the structures might have great differences at such a low temperature. In this work, the stress–strain curves were smoothed using the Savitzky–Golay method to eliminate the fluctuation, while keeping the simulation temperature stable at 300 K to simulate a real deformation process of graphene/eicosane composites.

Results

Equilibrium structures

Relative concentration of the equilibrium structures

The equilibrium structures of models A, B, C, and D after the equilibrium MD simulations are shown in Fig. 2. The equilibrium structure of each model is similar to its initial structure. In model A, the graphene sheets remain stacked together, while the graphene sheets in models B, C, and D stay separated by the eicosane molecules after the equilibrium MD simulations.

To analyze the distribution of eicosane molecules, relative concentration profiles of all the atoms in the z -direction were generated for the four models (Fig. 3). In Fig. 3, the two highest peaks in each model are the two graphene sheets. The relative concentration profiles show several peaks and troughs of eicosane in all four models, in addition to the graphene peaks. This indicates that eicosane forms several layers parallel to the graphene sheets, due to an adsorptive interaction with the graphene sheets. For ease of description, the layers are named based on their distances to the nearest of the two graphene sheets. Hence, the layers closest to the nearest graphene surface are named the first adsorption layers, the second closest layers are named the second adsorption layers, and so on (shown in Fig. 3). The peak height of each eicosane layer is related to its distance to the nearest graphene surface. The first adsorption layers have the largest peak heights, and as the distance from graphene surface increases, the peak heights of the adsorption layers decrease. This indicates that the adsorption effect of graphene drops as the distance from graphene gets larger.

In model A, the peaks of the fifth adsorption layers are too small to be distinguished from the bulk phase. This is where the bulk phase can be considered to begin. Thus, four obvious adsorption layers formed on each side of graphene surface in model A. The maximum range of influence for a single graphene sheet is about 20 \AA (from the graphene peak to the valley between the fourth layer and the bulk). In model B, eicosane forms several layers on the graphene surface, which is similar with model A. The length of the bulk phase in model B (about 10 \AA) is smaller than in model A (about 17 \AA), suggesting that

more eicosane molecules are layered because of their adsorption by graphene in model B. In models C and D, there are no bulk phases, as all the eicosane molecules are layered by adsorption. In model C, eicosane forms four distinct adsorption layers in the matrix, while model D only has three layers. Comparing model C with model D, the lowest eicosane peak in model D (the third adsorption layers) is higher than the lowest eicosane peak in model C (the fourth adsorption layers), indicating that eicosane lamination is stronger in model D than in model C. Based on all the analyses above, increasing the graphene dispersion leads to the increase in the overall influence on layering of the eicosane by the graphene sheets. This same influence is expected if polyethylene had been the matrix.

Eicosane radius of gyration

The distribution of the eicosane radii of gyration in all four models was calculated (Fig. 4). The radius of gyration in model A shows two peaks, where the top of the left peak is at 6.3 Å and the top of the right peak is at 7.3 Å. As the graphene separation increases (models B, C), the left peak drops and shifts to the right, while the right peak becomes higher. In model D, the left peak almost disappears, and only the right peak remains. As graphene dispersion increases, the eicosane conformations become more extended and uniform in the matrix (7.3 Å). The average radius of gyration in all four models was also calculated (Table 1). The average eicosane radius of gyration increases from 6.310 to 6.681 Å going from model A to D. Obviously, eicosane molecules are becoming more extended. The average radii of gyration for models C and D are similar, with a very small difference of 0.005 Å. Although polyethylene is much longer than eicosane, we propose the structure of polyethylene in the vicinity of graphene sheets should also be more extended as graphene dispersion increases in graphene/polyethylene composites.

Eicosane orientation

The orientations of the eicosane molecules were analyzed by calculating their angles with the z-direction. Of course, polyethylene will bend, loop, entangle, and also form crystalline lamella in a real composite's matrix. Here, eicosane is used only as a surrogate for the portion of the polyethylene near the

Table 1 Average radius of gyration for eicosane molecules in the four models

Model	Average radius of gyration (Å)
A	6.310
B	6.462
C	6.676
D	6.681

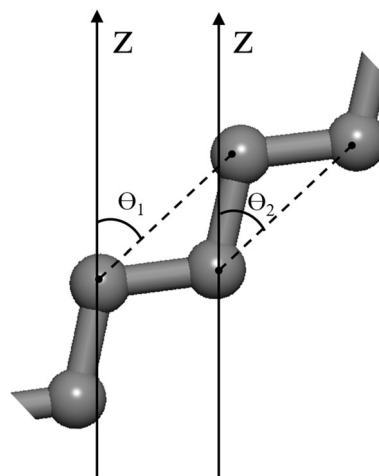


Figure 5 Angles with the z-direction for two segments in eicosane molecules.

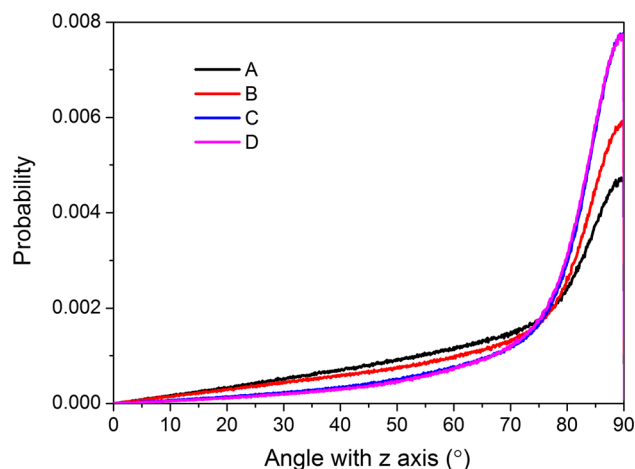


Figure 6 Distribution of eicosane segment angles with the z-direction in all four models.

graphene after equilibration. The carbon chain skeleton is divided into many segments, and the angle with the z-direction for every segment is calculated. The angles with the z-direction for two segments are shown in Fig. 5. In this figure, the H atoms

Table 2 Average angle with the z-axis for eicosane molecules in all four models

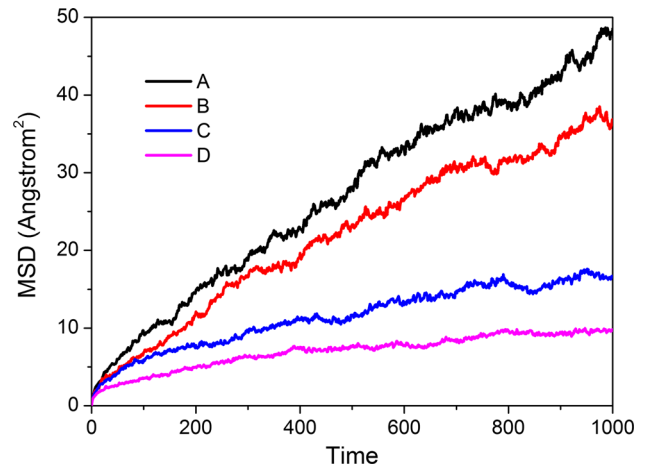
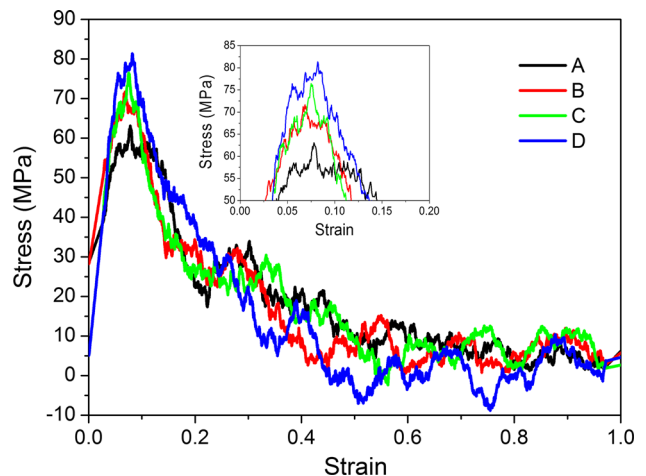
Model	Average angle with z-axis (°)
A	66.73
B	69.43
C	75.04
D	75.75

have been removed for clarity. The distribution of the angles for all the segments is used to represent the eicosane orientation as a surrogate polyethylene representation. The angle of 0° indicates that the molecules are parallel to the z-direction (perpendicular to the graphene surface), while 90° means that the molecules are parallel to the graphene surface.

The distributions of the eicosane angles with the z-direction for the four models are shown in Fig. 6. In all four models most angles are around 90° , suggesting that most molecules tend to be parallel to the graphene surface, because they are adsorbed to graphene. In model B, the distribution of angles around 90° becomes larger, and the distribution of angles below 76° becomes lower than those in model A. In turn, more angles in models C and D distribute close to 90° . This indicates that more eicosane molecules orient parallel to the graphene surfaces with the increase in the graphene dispersion. By extension, this is likely to also apply to polyethylene. Moreover, the distribution curves for angles in models C and D are almost coincident, indicating that the orientations of eicosane are similar in models C and D. To quantitatively analyze the orientation of eicosane in the four models, all the angles were averaged (Table 2). This average steadily increases from 66.73° to 75.75° with the increase in the graphene dispersion. Based on the above results, polyethylene molecules are expected to follow a trend where they better align parallel to the graphene surface in composites with a higher graphene dispersion.

Mean square displacement of eicosane molecules

To analyze the movement of eicosane molecules, the mean square displacement (MSD) of host molecules in the z-direction for the four models was calculated (Fig. 7). The MSD curve of eicosane molecules in the z-direction gradually becomes lower going from model A to model D. This illustrates that increasing

**Figure 7** MSD of eicosane in the z-direction in all four equilibrium models.**Figure 8** Stress–strain curves calculated for the four models (A–D) deformed in the uniaxial tension.

the graphene dispersion increasingly limits the movement of eicosane molecules in the direction perpendicular to the graphene surfaces. Polyethylene segments close to graphene are expected to exhibit this same trend.

Tensile deformation

Stress–strain behavior of graphene/eicosane composites

To analyze the effect of the graphene dispersion on the mechanical properties of these composites, uniaxial tensile simulations were performed. The stress–strain curves for the four models during the deformation process are shown in Fig. 8. In all models,

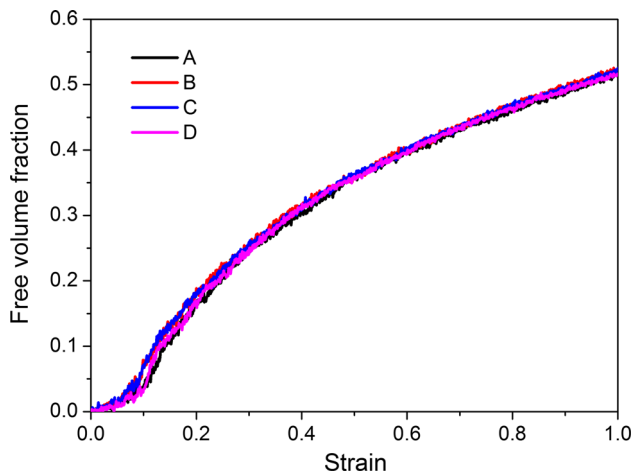


Figure 9 Free volume fraction for models A–D as a function of strain.

stress–strain curves proceed through the same stages, exhibiting elastic, yield, and softening regions during the deformation. The yield strains for models A to D are similar, around 8%. The yield stresses, however, increase steadily going from models A to D. These yield stresses are 63.1, 71.7, 76.5, and 81.4 MPa, respectively. Clearly, increasing graphene dispersion raises the yield stresses of the composites.

The yield stresses perpendicular to the graphene planes of all four models are very small. However, eicosane is a wax and not a structural material itself. C-20 molecules do not entangle significantly, and the short C-20 chains have modest attractions to each other over their short length, compared with the nominal 200,000 u typical of high-density linear polyethylene molecules. Polyethylenes exhibit crystallinity, which also helps to enhance moduli and yield stress. The temperature used for the stress strain curves was 300 K. At this temperature, eicosane molecules have sufficient thermal energy to allow them to slip past one another under a stress. This temperature is higher than the glass transition temperature of polyethylene. Hossain's work gives the same result about temperature [40]. Using eicosane as a polyethylene surrogate permits equilibrium structures to be obtained quickly and avoids bond-breaking reactions during the deformation, simplifying the simulations. So, although using eicosane in place of polyethylene leads to entirely unrealistic yield stresses, it does allow some simple factors to be observed about how graphene dispersion could influence composite structures. It also shows how deformations due to strain could also contribute in

graphene/polyethylene composites. This is the focus of this work.

Process of deformation

To study the graphene/eicosane composite deformation process, the free volume fraction was calculated during the uniaxial tensile simulation. When calculating the free volume, a virtual probe sphere with a radius of 3.4 Å was defined. Those areas of space that were accessible to the virtual probe sphere without touching any of the atomic points were defined as the free volume. All the free volumes were calculated using the alpha-shape method of Edelsbrunner and Mücke [42] as implemented in OVITO [43, 44]. Figure 9 shows the free volume fraction of all four models during the deformation. The free volume fraction curves of all four models are almost coincident, suggesting that the free volumes of the four models change similarly, since the same strain rate is applied for the four models during the deformation process. At the start of deformation, the free volume fraction increases slowly with the strain. Then, an abrupt rise in free volume fraction occurs at about 8% strain, followed by continual sharp increases with the strain. Comparing the free volume fraction curves with the stress–strain curves (Figs. 8 and 9), one observes the yield strains (in the stress–strain curves) coincide with the abrupt rises in the free volume fraction versus strain curves in all four models.

To explain the free volume fraction changes observed in Fig. 9, the dynamic structures of the composites during the deformation were analyzed. Several snapshots of the composites at different strains for models A–D are given in Fig. 10. The free volumes are also shown in each snapshot. The changes of the free volume in all four models are similar. Before the yield strain is reached for all four models (snapshots at 5% strain in Fig. 10), the free volume consists of many scattered and small voids in each model. After reaching the yield strain (snapshots at 10–20% strain in Fig. 10), the voids enlarge and coalesce into bigger voids. When the voids become large enough, the free volume morphs into a rod-like void (snapshots at 40% strain in Fig. 10). Finally, a lamellar void forms as the rod-like voids connect together (snapshots at 60% strain in Fig. 10). At this point, the composites are totally disconnected, and composite failures occur.

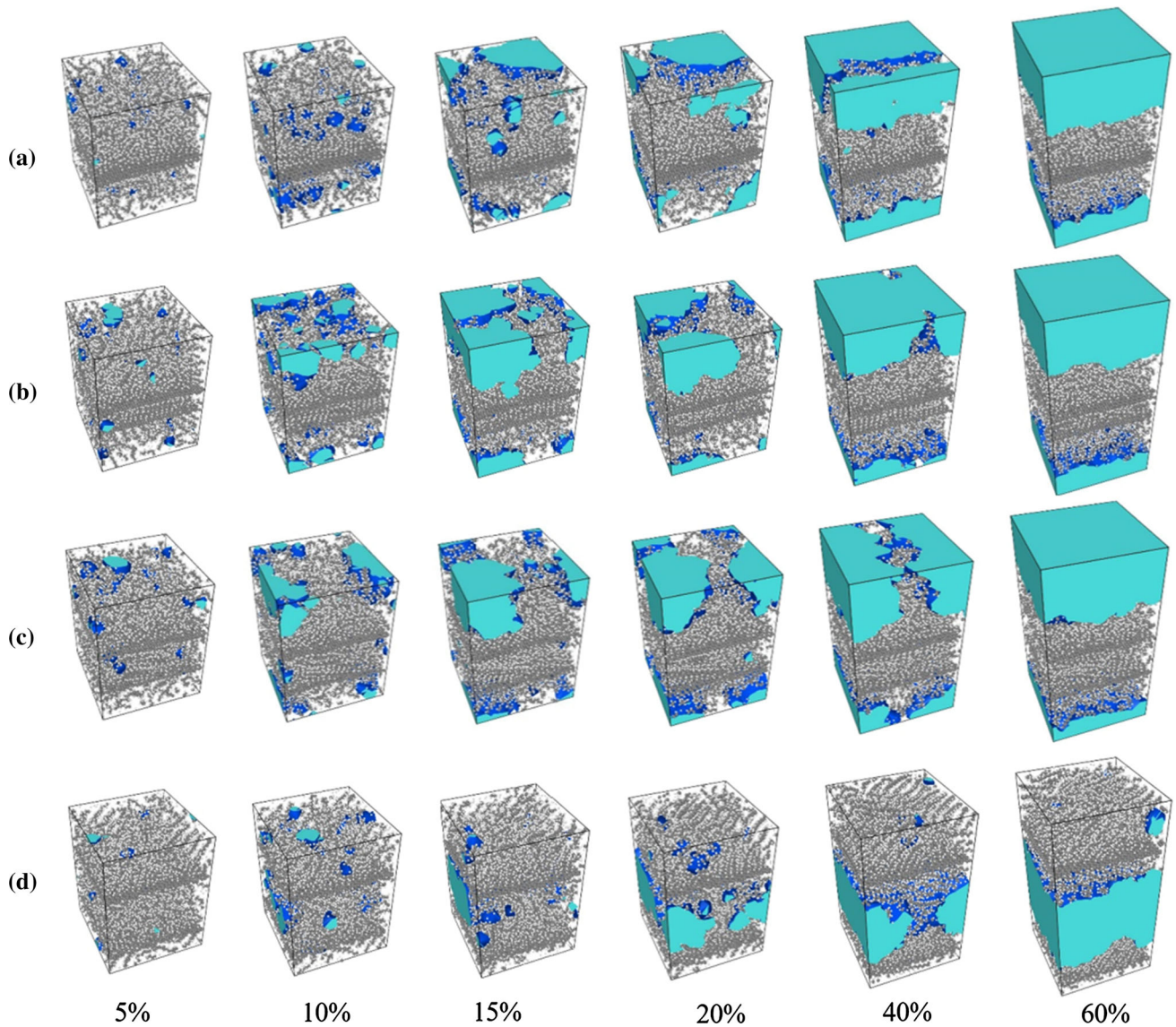
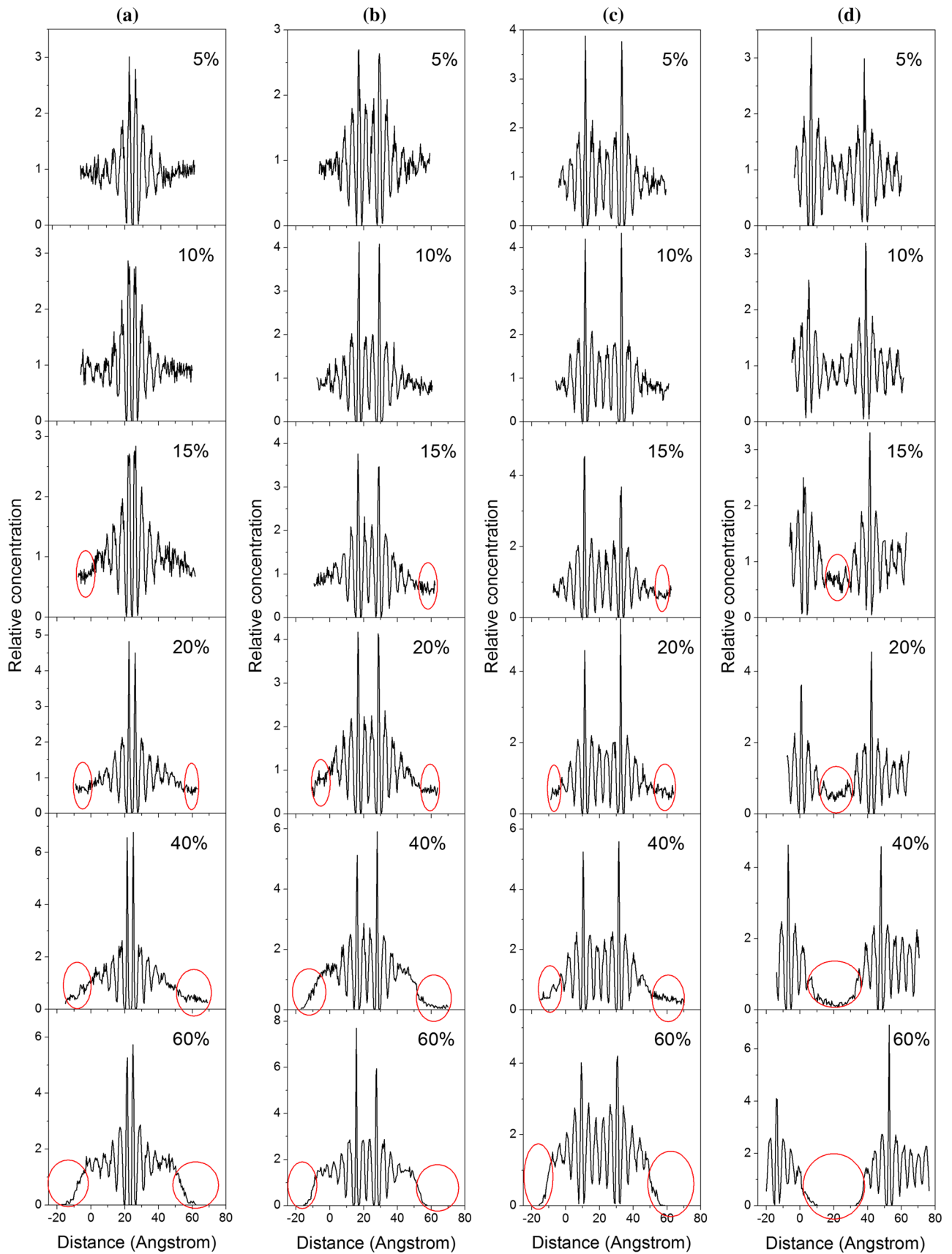


Figure 10 Snapshots of models A (a), B (b), C (c), and D (d) at increasing strains of 5–60% during the deformation.

Relative concentration profiles of models A–D during the deformation

The relative concentration profiles of all atoms in the z -direction at different strains for all four models were calculated and displayed (Fig. 11). In the relative concentration profiles at 5% strain, both adsorption layer peaks and the bulk phase are similar to the relative concentration of all atoms in equilibrium structures. This was found in all four models (Fig. 3), indicating the structures stay stable at this small strain in all models. At 10% strain, the concentration profiles basically stay unchanged compared with those at 5% strain. Thus, the structures

have not yet changed very much at 10%, although the voids start to become bigger after the 8% strain. When the strain reaches 15%, it is clear that the relative concentration profiles have changed in all four models. In model A, the relative concentration curve in the bulk phase is no longer horizontal, indicating that the void appears in the bulk phase, and it is big enough to damage the original bulk phase structure. The adsorption layer peaks are still stable and undamaged at 15% strain in model A. For model B at 15% strain, the relative concentration in the bulk phase is lower, and the adsorption layer peaks remain stable. Only the bulk phase is damaged, which is similar to model A. In model C at 15% strain,



◀ **Figure 11** Relative concentrations of all atoms in the z-direction for models A (a), B (b), C (c) and D (d) at different strains during the deformation. The voids in all four models at different strains are shown in red circles.

the fourth adsorption layers decrease in the relative concentration profile, since there is no bulk phase in the model C to respond to this deformation (Fig. 3). Thus, the fourth adsorption layers are damaged. In model D, the third adsorption layers disappear at 15% strain, which suggests that the voids damage these third adsorption layers. As strain increases from 15 to 40%, the voids in all four models enlarge (as shown in red circles in Fig. 11). Finally, at 60% strain, some regions of the relative concentration are zero, indicating that the voids in all four models merge into lamellar shapes, and the composites are completely broken.

Mean square displacement of eicosane molecules during the deformation

The movement of eicosane molecules during the deformation was analyzed. The MSD in the direction perpendicular to the graphene surface versus the strain were calculated (Fig. 12). The order of MSD for all four models during the deformation was the same as that of the equilibrium structures: $A > B > C > D$ (Figs. 7 and 12). Hence, graphene dispersion affects the motion of eicosane molecules during deformation. Eicosane molecules in model A have the largest diffusion rate. As graphene dispersion increases, eicosane movement becomes increasingly more inhibited during deformation of each model. As eicosane motion is inhibited, the yield stresses increase in the same order: $A < B < C < D$.

Graphene dispersion mechanism

“Adsorption solidification” in the equilibrium composites

Eicosane molecules are layered on the graphene surface in the equilibrium structures for models A, B, C, and D. Their conformations tend to be extended, their orientation tends to be parallel to the graphene surface, and their motions are inhibited. All these property changes resemble a “solidifying-like” phenomenon occurring. This solidification is due to

adsorptive interactions with the graphene surface. In our previous work [45], an interphase formed on the surface of overlapping graphene sheets in the graphene/epoxy resin composites, where the concentration, structures, and movements of the resin monomers were different from the bulk phase. Lacy et al. [46, 47] investigated the interaction between vinyl ester resin and overlapping graphene using MD simulations. A region adjacent to the graphene sheets had substantially different monomer ratios and concentrations from the bulk resin. The work of Shiu et al. [25] suggested that the density of epoxy polymers near the graphene surface is much higher than that of the bulk epoxy. The research of Hadden et al. [28] also showed that a ~ 10 -Å-thick interphase region formed on the graphene surface in the graphene/epoxy composites. All these results indicate that “adsorption solidification” is a common phenomenon in the graphene-based composites.

However, the range of this adsorption effect of the graphene is finite. It is limited to about 20 Å, which can only extend to four adsorption layers formed near the surface (Fig. 3). This means that the “adsorption solidification” should become increasingly important as more and more graphene sheets are added close together but with enough space between them to allow many molecular layers of the matrix molecules into the interlayer space, which minimizes the amount of the bulk phase. When two graphene sheets are stacked together (poor dispersion), the “adsorption solidification” can only occur in the region close to the graphene, and the graphene cannot interact with the matrix molecules far from the graphene surfaces. The molecules beyond 20 Å distance to the graphene are little affected by the graphene sheets. Thus, the host matrix is divided into two regions, the “adsorption solidification” phase and the bulk phase. Increasing the graphene dispersion decreases the bulk phase. When the graphene sheets are completely dispersed, the bulk phase will be the smallest or even disappear (models C and D), and the “adsorption solidification” phase becomes the main phase. The adsorption layer peak heights decrease going away from the graphene surface (Fig. 3). Hence, the degree of “adsorption solidification” of the first adsorption layers is the strongest, and this decreases going toward the bulk phase. In composites with low weight fractions of graphene, separately dispersing every graphene layer provides the highest graphene surface area, the highest

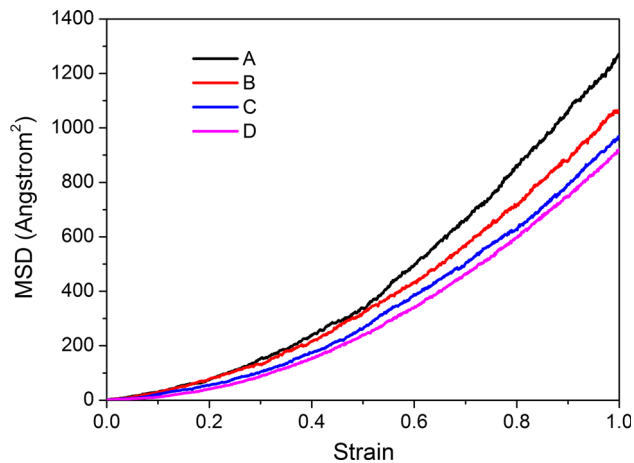


Figure 12 MSD of eicosane molecules in the z-direction in the four dispersion models during the deformation.

“adsorption solidification” for that given graphene weight fraction, and the most property enhancement based on this effect. Graphene orientation to a mechanical stress or to other graphenes is a separate effect. At some higher weight fraction, graphene can no longer be dispersed into fully separated platelets because sufficient matrix molecules will not be available to fill all the spaces. Practically, huge viscosity increases would also be induced at these high weight fractions.

“Adsorption solidification” effects during the deformation

During the deformation process, the damage occurs in the bulk phase in models A and B, in the fourth adsorption layers in model C, and in the third adsorption layers in model D (Fig. 11). In any model, damage always occurs in the region with weakest “adsorption solidification,” because more energy is needed to create void damage and disrupt structures with regions with stronger “adsorption solidification.” In models A and B, poor dispersion decreases the degree of the “adsorption solidification.” The bulk matrix phase in the matrix with the least adsorptive ordering is the “weakest” region. Thus, the bulk phase is destroyed first in models A and B. The adsorption layer is damaged first in models C and D, since there is no bulk phase. The yield stress increases with higher graphene dispersion. In models A and B, the “weaker” bulk phase is destroyed under the strain, while it is the fourth adsorption layer and the third adsorption layer with stronger “adsorption

solidification” which are damaged in models C and D, respectively. Thus, the yield stresses of model A and B are small. It is progressively more difficult to destroy the fourth layer in model C and then the third adsorption layers in model D. Consequently, the yield stress of model C is larger than for models A and B, and model D gives the largest yield stress. Higher graphene dispersion in polyethylene matrices should exhibit these same “adsorption solidification” effects with polymer chain segments aligning at graphene surfaces. Herein, only effects normal to graphene planes have been examined. In graphene/polyethylene composites, these surface adsorption interactions will enhance interfacial adhesion, allowing more effective matrix to reinforcement stress transfer when strains are imposed in any direction.

Conclusions

Models of graphene/eicosane composites with four different graphene dispersions were simulated to investigate the effects caused by the graphene dispersion. Eicosane was used as a surrogate for polyethylene. As the graphene dispersion increases, more host molecules become oriented in layers parallel to the graphene surface due to the adsorptive interactions with graphene. The radii of gyration for the host molecules are both more uniform and larger in the models with higher graphene dispersion. Also, the movement of host molecules becomes more inhibited. This process we term “adsorption solidification” of the composites. It becomes more widespread with increasing the graphene dispersion.

During uniaxial tensile deformation, the free volume increases slowly with strain in the elastic region, since small, scattered voids form at the start of deformation. After the yield strain, the free volume sharply increases, since the voids merge into larger voids, which damage the structure of the matrix. In every model, the damage always occurs in the region with the weakest “adsorption solidification.” The yield stress of the composites increases with the increase in graphene dispersion, since the “adsorption solidification” is stronger when the graphene sheets are more dispersed. In graphene/polyethylene composites, the “adsorption solidification” is also expected to be a contributing factor and have a similar influence as graphene dispersion increases.

Acknowledgements

This work is supported by the National Natural Science Foundation of China (51501226 and 51201183) and the Fundamental Research Funds for the Central Universities (15CX08009A, 15CX02066A and 14CX02221A). Shenghui Chen wishes to thank Dr. Thomas E. Lacy (Mississippi State University) for the helpful discussions with him.

Compliance with ethical standards

Conflict of interest The authors declare that they have no conflict of interest.

References

- [1] Novoselov KS, Geim AK, Morozov SV, Jiang D, Zhang Y, Dubonos SV, Grigorieva IV, Firsov AA (2004) Electric field effect in atomically thin carbon films. *Science* 306:666–669
- [2] Lee C, Wei X, Kysar JW, Hone J (2008) Measurement of the elastic properties and intrinsic strength of monolayer graphene. *Science* 321:385–388
- [3] Du X, Skachko I, Barker A, Andrei EY (2008) Approaching ballistic transport in suspended graphene. *Nat Nanotechnol* 3:491–495
- [4] Georgakilas V, Otyepka M, Bourlinos AB, Chandra V, Kim N, Kemp KC, Hobza P, Zboril R, Kim KS (2012) Functionalization of graphene: covalent and non-covalent approaches, derivatives and applications. *Chem Rev* 112:6156–6214
- [5] Mittal G, Dhand V, Rhee KY, Park S-J, Lee WR (2015) A review on carbon nanotubes and graphene as fillers in reinforced polymer nanocomposites. *J Ind Eng Chem* 21:11–25
- [6] Huang X, Qi X, Boey F, Zhang H (2012) Graphene-based composites. *Nature* 41:666–686
- [7] Kuilla T, Bhadra S, Yao DH, Kim NH, Bose S, Lee JH (2010) Recent advances in graphene based polymer composites. *Prog Polym Sci* 35:1350–1375
- [8] Singh V, Joung D, Zhai L, Das S, Khondaker SI, Seal S (2011) Graphene based materials: past, present and future. *Prog Mater Sci* 56:1178–1271
- [9] Hu K, Kulkarni DD, Choi I, Tsukruk VV (2014) Graphene-polymer nanocomposites for structural and functional applications. *Prog Polym Sci* 39:1934–1972
- [10] Zhao X, Zhang Q, Chen D, Lu P (2010) Enhanced mechanical properties of graphene-based poly(vinyl alcohol) composites. *Macromolecules* 43:2357–2363
- [11] Liang JJ, Wang Y, Huang Y, Ma YF, Liu ZF, Cai JM, Zhang CD, Gao HJ, Chen YS (2009) Electromagnetic interference shielding of graphene/epoxy composites. *Carbon* 47:922–925
- [12] Pang HA, Chen C, Zhang YC, Ren PG, Yan DX, Li ZM (2011) The effect of electric field, annealing temperature and filler loading on the percolation threshold of polystyrene containing carbon nanotubes and graphene nanosheets. *Carbon* 49:1980–1988
- [13] Song PG, Gao ZH, Cai YZ, Zhao LP, Fang ZP, Fu SY (2011) Fabrication of exfoliated graphene-based polypropylene nanocomposites with enhanced mechanical and thermal properties. *Polymer* 52:4001–4010
- [14] Rafiee MA, Rafiee J, Srivastava I, Wang Z, Song H, Yu Z-Z, Koratkar N (2010) Fracture and fatigue in graphene nanocomposites. *Small* 6:179–183
- [15] Ramanathan T, Abdala AA, Stankovich S, Dikin DA, Herrera-Alonso M, Piner RD et al (2008) Functionalized graphene sheets for polymer nanocomposites. *Nat Nanotechnol* 3:327–331
- [16] Si Y, Samulski ET (2008) Synthesis of water soluble graphene. *Nano Lett* 8:1679–1682
- [17] Si Y, Samulski ET (2008) Exfoliated graphene separated by platinum nanoparticles. *Chem Mater* 20:6792–6797
- [18] Zacharia R, Ulbricht H, Hertel T (2004) Interlayer cohesive energy of graphite from thermal desorption of polyaromatic hydrocarbons. *Phys Rev B* 69:155406
- [19] Tang LC, Wan YJ, Yan D, Pei YB, Zhao L, Li YB, Wu LB, Jiang JX, Lai GQ (2013) The effect of graphene/epoxy composites on the mechanical properties of graphene/epoxy composites. *Carbon* 60:16–27
- [20] Kim H, Miura Y, Macosko CW (2010) Graphene/polyurethane nanocomposites for improved gas barrier and electrical conductivity. *Chem Mater* 22:3441–3450
- [21] Yang SY, Lin WN, Huang YL, Tien HW, Wang JY, Ma CCM, Li SML, Wang YS (2011) Synergetic effects of graphene platelets and carbon nanotubes on the mechanical and thermal properties of epoxy composites. *Carbon* 49:793–803
- [22] Montazeri A, Rafii-Tabar H (2011) Multiscale modeling of graphene- and nanotube-based reinforced polymer nanocomposites. *Phys Lett A* 375:4034–4040
- [23] Ebrahimi S, Ghafoori-Tabrizi K, Rafii-Tabar H (2012) Multi-scale computational modelling of the mechanical behaviour of the chitosan biological polymer embedded with graphene and carbon nanotube. *Comput Mater Sci* 53:347–353
- [24] Zhang T, Xue Q, Zhang S, Dong M (2012) Theoretical approaches to graphene and graphene-based materials. *Nano Today* 7:180–200
- [25] Shiu SC, Tsai JL (2014) Characterizing thermal and mechanical properties of graphene/epoxy nanocomposites. *Compos B* 56:691–697

- [26] Rahman R, Haque A (2013) Molecular modeling of cross-linked graphene–epoxy nanocomposites for characterization of elastic constants and interfacial properties. *Compos B* 54:353–364
- [27] Rahman R, Foster JT (2014) Deformation mechanism of graphene in amorphous polyethylene: a molecular dynamics based study. *Comput Mater Sci* 87:232–240
- [28] Hadden CM, Klimek-McDonald DR, Pineda EJ, King JA, Reichanadter AM, Miskioglu I, Gowtham S, Odegard GM (2015) Mechanical properties of graphene nanoplatelet/carbon fiber/epoxy hybrid composites: multiscale modeling and experiments. *Carbon* 95:100–112
- [29] Lv C, Xue Q, Xia D, Ma M, Xie J, Chen H (2010) Effect of chemisorption on the interfacial bonding characteristics of graphene–polymer composites. *J Phys Chem C* 114:6588–6594
- [30] Lv C, Xue Q, Xia D, Ma M (2012) Effect of chemisorption structure on the interfacial bonding characteristics of graphene–polymer composites. *Appl Surf Sci* 258:2077–2082
- [31] Xiong QL, Tian XG (2015) Atomistic modeling of mechanical characteristics of CNT-polyethylene with interfacial covalent interaction. *Journal of Nanomaterials* 1-9
- [32] Liu F, Hu N, Ning H, Liu Y, Li Y, Wu L (2015) Molecular dynamics simulation on interfacial mechanical properties of polymer nanocomposites with wrinkled graphene. *Comput Mater Sci* 108:160–167
- [33] Rissanou AN, Power AJ, Harmandaris V (2015) Structural and dynamical properties of polyethylene/graphene nanocomposites through molecular dynamics simulations. *Polymer* 7:390–417
- [34] Rissanou AN, Harmandaries V (2014) Dynamics of various polymer–graphene interfacial systems through atomistic molecular dynamics simulations. *Soft Matter* 10:2876–2888
- [35] Plimpton S (1995) Fast parallel algorithms for short-range molecular dynamics. *J Comput Phys* 117:1–19
- [36] Sun H (1994) Force field for computation of conformational energies, structures, and vibrational frequencies of aromatic polyesters. *J Comput Chem* 15:752–768
- [37] Yang S, Yu S, Cho M (2013) Influence of Thrower–Stone–Wales defects on the interfacial properties of carbon nanotube/polypropylene composites by a molecular dynamics approach. *Carbon* 55:133–143
- [38] Fan HB, Yuen MMF (2007) Material properties of cross-linked epoxy resin compound predicted by molecular dynamics simulation. *Polymer* 48:2174–2178
- [39] Yang L, Srolovitz DJ, Yee AF (1997) Extended ensemble molecular dynamics method for constant strain rate uniaxial deformation of polymer systems. *J Chem Phys* 107:4396–4407
- [40] Hossain D, Tschopp MA, Ward DK, Bouvard JL, Wang P, Horstemeyer MF (2010) Molecular dynamics simulations of deformation mechanisms of amorphous polyethylene. *Polymer* 51:6071–6083
- [41] Jiang Q, Tallury SS, Qiu YP, Pasquinelli MA (2014) Molecular dynamics simulations of the effect of the volume fraction on unidirectional polyimide–carbon nanotube nanocomposites. *Carbon* 67:440–448
- [42] Edelsbrummer H, Mücke EP (1994) Three-dimensional alpha shapes. *ACM Trans Graph* 13:63–100
- [43] Stukowski A (2014) Computational analysis methods in atomistic modeling of crystals. *JOM* 66:399–407
- [44] Stukowski A (2010) Visualization and analysis of atomistic simulation data with OVITO—the Open Visualization Tool. *Model Simul Mater Sci Eng* 18:015012
- [45] Chen SH, Sun SQ, Gwaltney SR, Li CL, Wang XM, Hu SQ (2015) Molecular dynamics simulations of the interaction between carbon nanofiber and epoxy resin monomers. *Acta Polym Sin* 10:1158–1164
- [46] Nouranian S, Jang C, Lacy TE, Gwaltney SR, Toghiani H, Pittman CU Jr (2011) Molecular dynamics simulations of vinyl ester resin monomer interactions with a pristine vapor-grown carbon nanofiber and their implications for composite interphase formation. *Carbon* 49:3219–3232
- [47] Jang C, Nouranian S, Lacy TE, Gwaltney SR, Toghiani H, Pittman CU Jr (2012) Molecular dynamics simulations of oxidized vapor-grown carbon nanofiber surface interactions with vinyl ester resin monomers. *Carbon* 50:748–760